INL/JOU-24-76943-Revision-0

Effects of Irradiation Damage on the Hardness and Elastic Properties of Quaternary and High Entropy Transition Metal Diborides

September 2024

Changing the World's Energy Future

Amey Rajendra Khanolkar, Yang Liu, Amit Datye, Yan Zhang, Cody A. Dennett, Weiming Guo, William J. Weber, Hua-Tay Lin, Yanwen Zhang

Idaho National Laboratory

INL is a U.S. Department of Energy National Laboratory operated by Battelle Energy Alliance, LLC

DISCLAIMER

This information was prepared as an account of work sponsored by an agency of the U.S. Government. Neither the U.S. Government nor any agency thereof, nor any of their employees, makes any warranty, expressed or implied, or assumes any legal liability or responsibility for the accuracy, completeness, or usefulness, of any information, apparatus, product, or process disclosed, or represents that its use would not infringe privately owned rights. References herein to any specific commercial product, process, or service by trade name, trade mark, manufacturer, or otherwise, does not necessarily constitute or imply its endorsement, recommendation, or favoring by the U.S. Government or any agency thereof. The views and opinions of authors expressed herein do not necessarily state or reflect those of the U.S. Government or any agency thereof.

INL/JOU-24-76943-Revision-0

Effects of Irradiation Damage on the Hardness and Elastic Properties of Quaternary and High Entropy Transition Metal Diborides

Amey Rajendra Khanolkar, Yang Liu, Amit Datye, Yan Zhang, Cody A. Dennett, Weiming Guo, William J. Weber, Hua-Tay Lin, Yanwen Zhang

September 2024

Idaho National Laboratory
Idaho Falls, Idaho 83415

http://www.inl.gov

Prepared for the
U.S. Department of Energy
Under DOE Idaho Operations Office
Contract DE-AC07-05ID14517

ACCEPTED MANUSCRIPT
Journal of Applied Physics
AIP Publishing
This is the author's peer reviewed, accepted manuscript. However, the online version of record will be different from this version once it has been copyedited and typeset.
PLEASE CITE THIS ARTICLE AS DOI: 10.1063/5.0206224

Effects of Irradiation Damage on the Hardness and Elastic Properties of Quaternary and High Entropy Transition Metal Diborides

Amey Khanolkar[1*], Amit Datye[2], Yan Zhang[3,4], Cody A. Dennett[5], Weiming Guo[3], Yang Liu[3], William J. Weber[6], Hua-Tay Lin[3], and Yanwen Zhang[1,7*]

[1] *Condensed Matter and Materials Physics Group, Idaho National Laboratory, Idaho Falls, ID 83415 USA*
[2] *Department of Mechanical Engineering and Materials Science, Yale University, New Haven, CT 06520 USA*
[3] *School of Electromechanical Engineering, Guangdong University of Technology, Guangzhou, 510006 China*
[4] *School of Mechanical and Electrical Engineering, Shaoxing University, Shaoxing, 312000, China*
[5] *Department of Nuclear Science and Engineering, Massachusetts Institute of Technology, Cambridge, MA 02139 USA*
[6] *Department of Materials Science & Engineering, University of Tennessee, Knoxville, TN 37996, USA*
[7] *Department of Mechanical and Materials Engineering, Smith Engineering, Queen's University, Kingston, Ontario, K7L 2N8, Canada*

ABSTRACT

Multi-principal component transition metal diborides represent a class of high-entropy ceramics (HECs) that have received considerable interest in recent years owing to their promising properties for extreme environment applications that include thermal/ environmental barriers, hypersonic vehicles, turbine engines, and next-generation nuclear reactors. While the addition of chemical disorder through the random distribution of transition metal (TM) elements on the cation sublattice has offered opportunities to tailor elastic stiffness and hardness, the effects of irradiation-induced structural damage on the physical properties of these complex materials has remained largely unexplored. To this end, changes in the hardness and elastic moduli of a high entropy TM diboride $(Hf_{0.2}Nb_{0.2}Ta_{0.2}Ti_{0.2}Zr_{0.2})B_2$ and three of its quaternary subsets following irradiation with 10 MeV gold (Au) ions to fluences of up to 6×10^{15} Au cm^{-2} are investigated at the micrometer and sub-micrometer length-scales via the dispersion of laser-generated surface acoustic waves (SAW) and nanoindentation, respectively. The nanoindentation measurements show that the TM diborides exhibit an initial increase in hardness following irradiation with energetic Au ions, with a subsequent decrease in hardness following further irradiation. One quaternary composition, $(Hf_{1/3}Ta_{1/3}Ti_{1/3})B_2$ exhibits a notable exception to the trend and continues to exhibit an increase in hardness with ion irradiation fluence. Although differences in the absolute values of the effective elastic moduli obtained from the measured SAW dispersion and nanoindentation are observed (and attributed to microstructural variations at the measurement length-scale), both techniques yield similar trends in the form of an initial reduction and subsequent saturation in the elastic modulus with increasing ion irradiation fluence. The quaternary TM diboride $(Hf_{1/3}Ta_{1/3}Ti_{1/3})B_2$ again exhibits a departure from this trend. The high entropy TM diboride $(Hf_{0.2}Nb_{0.2}Ta_{0.2}Ti_{0.2}Zr_{0.2})B_2$ exhibits the greatest recovery in hardness and modulus when irradiated to high ion fluences following initial changes at low fluence, indicating superior resistance to radiation-induced damage over its quaternary counterparts. Opportunities for designing HECs with superior hardness and modulus for enhanced radiation resistance (compared to their single constituent counterparts) by tailoring chemical disorder and bond character in the lattice are discussed.

Keywords: High entropy ceramics; transition metal diborides; elastic properties; hardness; radiation damage; nanoindentation; transient grating spectroscopy.

[*] To whom correspondence should be addressed:
Amey Khanolkar (Amey.Khanolkar@inl.gov)
Yanwen Zhang (Yanwen.Zhang@QueensU.ca)

Journal of Applied Physics
AIP Publishing
ACCEPTED MANUSCRIPT
This is the author's peer reviewed, accepted manuscript. However, the online version of record will be different from this version once it has been copyedited and typeset.
PLEASE CITE THIS ARTICLE AS DOI: 10.1063/5.0206224

1. INTRODUCTION

High entropy materials (HEMs) are a class of materials comprised of typically single phase solid solution alloys with approximately equiatomic concentrations of constituent elements that have garnered significant interest over the past two decades from the materials research community owing to their potential for superior performance in extreme environments [1-5]. Although the majority of research on HEMs has focused on compositionally complex metal alloys, the concept of HEMs has been extended to ceramics, i.e., high-entropy ceramics (HECs), with an aim of developing of high entropy ceramics with superior physical properties such as higher hardness, low thermal conductivity, enhanced strength at elevated temperature, as well as radiation resistance, all of which are desired for materials deployed in applications demanding thermal, environmental, or radiation protection, such as next-generation nuclear reactors, hypersonic vehicles, thermoelectric power generation, catalysis, and advanced gas turbines [6, 7]. The vast composition space of HECs has not just motivated the study of advanced ceramics with designed responses but has also set the stage for the discovery of new physics beyond the realm of conventional ceramics [6]. Investigations on HECs were first reported in entropy-stabilized oxides [8], and have since expanded to borides [9, 10], carbides [11-13], nitrides [14-16], sulfides [17], and silicides [18, 19]. HECs have been shown to retain their crystalline phase under elevated temperature [20-22] and pressure [23, 24] environments, as well as under radiation fields comprised of energetic ions [10, 25, 26]. While most of experimental investigations on HECs have focused on synthesis and microstructure characterization [6, 27-29], there remains a limited understanding of the correlation between compositional complexity, atomic-level disorder, and the resulting physical properties of HECs [10].

The mechanical properties of HECs are a vital performance metric, particularly at elevated temperatures necessitated by several technological applications. Besides their sensitivity to temperature, the mechanical properties of HECs influenced by microstructure-related factors such as the residual porosity, grain size, and impurities such as undesired oxides [7]. The mechanical/elastic properties of ceramics are also strongly affected by the presence and accumulation of irradiation-induced defects (such as vacancies, interstitials, and voids) [30]. While conventional ceramics possess high stiffness and superior hardness, the presence of covalent bonds in ceramics make them highly brittle [31]. In this regard, HECs show promise in tailoring the ductility of ceramics through the introduction of metal atoms in the cation sublattice that provide valence electrons to raise the toughness of the material, while the anion sublattice forms a covalent bonding network to build hardness [31]. First principles investigations have shown that the valence electron concentration (VEC, defined as the number of electrons per formula unit) of the metal cations and the relative electronegativity difference between the cation and anion sublattices serve as key descriptors for the optimization of the balance between hardness and toughness in ceramics [31]. Besides the VEC and electronegativity difference, the differing sizes of metal cations also offers a means of enhancing the mechanical properties of HECs, via lattice distortions introduced by the size differences [6, 32, 33]. Experimentally, the characterization of the mechanical properties of HECs has included flexural strength measurements using bend tests and fracture toughness measurements using notched crack extension specimens [7, 34, 35]. The hardness of HECs (that include high entropy carbides and borides) is another mechanical property that has been commonly reported using micro- or nanoindentation [12, 36, 37]. Despite recent reports of the promising radiation resistance of HECs [10, 25, 26], studies that correlate radiation damage in HECs with changes in mechanical properties have been lacking.

In this study, we aim to address this knowledge gap by investigating the influence of irradiation-induced microstructural damage on the hardness and elastic moduli of a senary high entropy boride (HEB) and three quaternary subsets of the high entropy diboride. The metal cation sublattice in the HECs investigated here include Group IVB, VB, and VIB transition metal (TM) elements that crystallize in the hexagonal AlB_2 phase [10]. The quaternary transition metal diborides and the high entropy diboride were

AIP Publishing

Journal of Applied Physics

ACCEPTED MANUSCRIPT

This is the author's peer reviewed, accepted manuscript. However, the online version of record will be different from this version once it has been copyedited and typeset.

PLEASE CITE THIS ARTICLE AS DOI: 10.1063/5.0206224

synthesized using spark plasma sintering (SPS) followed by hot pressing (HP) [10]. Irradiation damage was introduced by exposing the TM diboride samples to 10 MeV gold (Au) ions at room temperatures to four fluences (ranging from 1×10^{14} to 6×10^{15} Au cm^{-2}). Measurements of elastic properties were conducted with two approaches – nanoindentation to obtain elastic (Young's modulus, *E*) and plastic (hardness) properties during the loading and unloading processes [38]; and the laser-induced transient grating spectroscopy (TGS) technique [39, 40] where the Young's modulus (E) and shear modulus (G) were obtained from the measured dispersion of surface acoustic waves (SAWs). The absolute values of elastic moduli as well as relative trends in the elastic properties as a function of irradiation dose and chemical composition obtained by the two methods are discussed. The observed changes in elastic properties and hardness are correlated with recently-reported characterization of the microstructure of the irradiated HEBs [10]. This work provides new insight into the evolution of elastic properties resulting from irradiation-induced defects in the microstructure of HEBs. Perspectives on designing radiation-tolerant ceramics that retain (or even enhance) elastic stiffness and hardness under irradiation are also provided.

2. MATERIALS AND METHODS

2.1. Material Synthesis

Bulk samples composed of three quinary HEBs with equiatomic concentrations of Group IVB, VB, and VIB transition metal elements (i.e., $(Hf_{1/3}Ta_{1/3}Ti_{1/3})B_2$, $(Hf_{1/3}Ta_{1/3}Zr_{1/3})B_2$, and $(Hf_{1/3}Ti_{1/3}Zr_{1/3})B_2$) and one senary high entropy diboride (i.e., $(Hf_{0.2}Nb_{0.2}Ta_{0.2}Ti_{0.2}Zr_{0.2})B_2$) were synthesized using spark plasma sintering (SPS) followed by hot pressing (HP) of raw-oxide based powders in equimolar ratios with boron carbide (B_4C). X-ray diffraction (XRD) and energy dispersive X-ray spectroscopy (EDS) were used to check for traces of secondary phases associated with oxygen, carbon, or other impurities. While the XRD spectra exhibited distinctive peaks associated with the AlB_2 hexagonal lattice, several low intensity peaks, possibly attributed to minor secondary oxide phases, were also detected. EDS spectroscopy confirmed the presence of minor quantities of secondary oxide phases, typically located at grain boundaries. Details of the sample synthesis and XRD/EDS characterization have been reported previously [10]. It should be noted that the presence of undesired secondary oxide phases in the microstructure can influence the mechanical properties of the diborides [7]. The density of the sintered quinary and senary diborides was measured using the Archimedes principle. The relative density measured on these samples is comparable to that previously reported on similar high-entropy transition metal diboride samples produced via sintering techniques [9]. The deviation from 100% density is attributed primarily to the presence of porosity in the samples, owing to prior observations of micrometer-scale porosity in cross-sectional scanning electron microscopy (SEM) images [9]. Table 1 lists the compositions of each of the four samples investigated in this study, along with their theoretical and measured mass density. The sintered monoliths were polished prior to ion irradiation. The average surface roughness of the as-sintered $(Hf_{1/3}Ta_{1/3}Zr_{1/3})B_2$ was measured to be ~28 nm using a Veeco Wyno NT9100 optical surface profiler (Veeco Instruments Inc., Tucson, USA).

Table 1. Compositions and theoretical/ measured density of the transition metal diboride samples.

Composition	Theoretical density (g/cm^3)	Measured density (g/cm3)	Percent relative density (%)
$(Hf_{1/3}Ta_{1/3}Ti_{1/3})B_2$	9.52	8.95	94.0
$(Hf_{1/3}Ta_{1/3}Zr_{1/3})B_2$	9.83	9.43	95.9
$(Hf_{1/3}Ti_{1/3}Zr_{1/3})B_2$	7.45	7.24	97.2
$(Hf_{0.2}Nb_{0.2}Ta_{0.2}Ti_{0.2}Zr_{0.2})B_2$	8.18	7.69	94.0

AIP Publishing
Journal of Applied Physics
ACCEPTED MANUSCRIPT
This is the author's peer reviewed, accepted manuscript. However, the online version of record will be different from this version once it has been copyedited and typeset.
PLEASE CITE THIS ARTICLE AS DOI: 10.1063/5.0206224

2.2. Ion irradiations

The samples were irradiated with 10 MeV Au ions at room temperature at the Ion Beam Materials Laboratory at the University of Tennessee Knoxville [41] to four fluences (1×10^{14}, 5×10^{14}, 2×10^{15} and 6×10^{15} Au cm^{-2}) with a constant ion flux of ~9.26×10^{11} Au cm^{-2}s^{-1}. Details of the ion irradiation experiments have been reported previously [10]. The Stopping Range of Ions in Matter (SRIM) [42] in full cascade mode [43] was used to estimate the atomic displacement damage profiles in the TM diborides. The displacement damage and ion implantation depth profiles calculated using SRIM have been reported previously [10]. The SRIM calculations predicted peak displacement dose that ranged between ~0.44 – 0.67 displacements per atom (dpa) at the lowest fluence of 1×10^{14} Au/cm^2 and ~25.6 – 34.3 dpa at the highest fluence of 6×10^{15} Au/cm^2. The SRIM results suggest that most ion-induced damage occurs within ~ 1.6 µm of the surface with the peak damage located at ~ 0.9 µm [10]. The peak damage under the four ion fluences is provided in Table 2. The average surface roughness of the $(Hf_{1/3}Ta_{1/3}Zr_{1/3})B_2$ sample irradiated to a fluence of 5×10^{14} Au cm^{-2} was measured at ~48 nm, indicating a ~71% increase in surface roughness following irradiation.

Table 2. SRIM predicted peak dose (dpa) under different ion fluences

Fluence (Au cm^{-2})	**1×10^{14}**	**5×10^{14}**	**2×10^{15}**	**6×10^{15}**
$(Hf_{1/3}Ta_{1/3}Ti_{1/3})B_2$	0.44	2.21	8.85	26.6
$(Hf_{1/3}Ta_{1/3}Zr_{1/3})B_2$	0.57	2.86	11.4	34.3
$(Hf_{1/3}Ti_{1/3}Zr_{1/3})B_2$	0.46	2.31	9.24	27.7
$(Hf_{0.2}Nb_{0.2}Ta_{0.2}Ti_{0.2}Zr_{0.2})B_2$	0.43	2.13	8.54	25.6

2.3. Hardness and elastic modulus measurements using nanoindentation

The nanoindentation experiments were carried out using an iNano system (KLA, Milpitas, USA), equipped with a Berkovich diamond tip (Micro Star Technologies, Huntsville, USA). The elastic modulus and hardness of the TM diboride samples were measured using a modified Continuous Stiffness Measurement (CSM) method with enhanced surface detection criteria [38, 44, 45] at a constant strain rate of 0.5/s and up to a peak load of 50 mN. A schematic representation of the nanoindentation experiment is illustrated in Figure 1(a). The contact stiffness between the indented and the sample is given by [46],

$$S = \frac{dP}{dh} = \frac{2}{\sqrt{\pi}} E_r \sqrt{A}, \tag{1}$$

where P is the indentation load, h is the indentation depth, and A is the projected contact area. E_r is the reduced modulus, which combines the elastic deformation of the sample and the indenter through the relation $\frac{1}{E_r} = \frac{1-\nu^2}{E} + \frac{1-\nu_i^2}{E_i}$, where (E, ν) and (E_i, ν_i) are the Young's modulus and Poisson's ratio of the sample and the indenter, respectively. Since the TM diboride samples are expected to be elastically isotropic [47], the effective modulus is defined as [48],

$$E_{eff} = \frac{E}{(1-\nu^2)}. \tag{2}$$

In the modified CSM scheme, the hardness was calculated as a function of penetration depth using the relation, $H = {}^{P}/_{A_c}$, where P is the measured load and A_c is the contact area which is a function of the contact depth h_c. A standard fused silica calibration samples of known hardness and modulus was used to

AIP Publishing
Journal of Applied Physics
ACCEPTED MANUSCRIPT
This is the author's peer reviewed, accepted manuscript. However, the online version of record will be different from this version once it has been copyedited and typeset.
PLEASE CITE THIS ARTICLE AS DOI: 10.1063/5.0206224

obtain the area function with respect to the contact depth as outlined in the Oliver-Pharr method [38] following the equation: $h_c = h - \varepsilon \frac{P}{S}$, where h is the indentation depth and ε is a constant that depends on the intender geometry [49]. Based on the data from the fused silica calibration samples, hardness values obtained at penetration depths less than 75 nm from the surface were not considered, due to various effects such as tip rounding (wherein complete plasticity for hardness measurements is not achieved) and tip-sample surface contact (i.e., surface asperities). The elastic modulus, however, is accurate at penetration depths as low as 50 nm. For consistency, however, the hardness and modulus measurements were com computed for each indentation depth and averaged over the 75 – 225 nm penetration depth range. Although the Nix-Gao model has been widely applied to accurately determine hardness by correcting for indentation size effects that result in a depth-dependent hardness [50], the Oliver-Pharr model was deemed adequate to extract hardness from the measured load-displacement curves since the hardness obtained using this approach showed a weak dependence with depth in the 75 – 225 nm range (the depth range over which the measured hardness was averaged). Figure 1(b) shows a representative load versus displacement curve acquired on the as-sintered $(Hf_{0.2}Nb_{0.2}Ta_{0.2}Ti_{0.2}Zr_{0.2})B_2$ high entropy diboride sample during the loading, dwell, and unloading phases. An average of 16 indents per sample were performed to determine the Young's modulus and hardness.

2.4. Young's and shear modulus measurements using transient grating spectroscopy

The laser-induced transient grating spectroscopy (TGS) technique [39, 40] was used as a non-contact, non-destructive complimentary method to nanoindentation for measuring the Young's and shear moduli of the TM diboride samples, and is one of several pump-probe laser ultrasonic techniques [51]. The TGS technique is an all-optical approach for generating surface acoustic waves (SAWs) with a defined wave vector and detecting their phase velocity in homogeneous and layered elastic half-spaces [52, 53]. In this approach, two excitation laser pulses derived from the same laser source ($\lambda_e = 532$ nm wavelength, 440 ps pulse duration, ~2.5 μJ total pulse energy at the sample, and 1 kHz repetition rate) are spatially and temporally overlapped on the surface of the sample to a ~500 μm diameter spot at the $1/e^2$ intensity level (schematic shown in Figure 1(c)). Absorption of the laser energy by the TM diboride sample induces rapid thermal expansion, which leads to the generation of counterpropagating SAWs with a wavelength λ_S defined by interference fringe pattern created by the crossed laser pulses on the sample surface. The period of the interference is controlled by a phase mask pattern that splits the incident laser beam into two excitation beams along the ± 1 diffraction orders [53]. The SAW wavelength λ_S is determined by the crossing angle θ of the excitation laser pulses (and consequently, by the periodicity of the interference fringe pattern), using the relation,

$$\lambda_S = \frac{\lambda_e}{2\sin\left(\theta/2\right)} \tag{4}$$

SAW detection is accomplished using a quasi-continuous wave (CW) probe laser beam (577 nm wavelength, ~10 mW average power at the sample) focused on the center of the excitation pattern to a spot of ~200 μm diameter. The probe beam is diffracted by the SAW surface ripples and strain-induced refractive index variations. The dual-phase heterodyne phase detection scheme was used for SAW detection [54]. In this scheme, the diffracted beam is overlapped with the reflected reference beam (Figure 1(c)) and directed onto a fast avalanche photodiode (Hamamatsu C5658, Hamamatsu Photonics, Japan) with a 1 GHz bandwidth. The signal is recorded using an oscilloscope and averaged over 10,000 repetitions. A representative time-domain TGS signal acquired on the quinary TM diboride $(Hf_{1/3}Ti_{1/3}Zr_{1/3})B_2$ irradiated to a fluence of 1×10^{14} Au cm^{-2} at a SAW wavelength of $\lambda_S = 7$ μm is shown in Figure 1(d). The initial sharp increase in the signal corresponds to the excitation pulses arriving at the sample. The slowly decay component is due to the diffusion of the "thermal grating" created by the interference fringe pattern [53, 55]. The inset of Figure 1(d) shows the high frequency oscillations associated with the SAW packet. The Fourier spectrum of the oscillations corresponding to the signal in

ACCEPTED MANUSCRIPT

Journal of Applied Physics

AIP Publishing

This is the author's peer reviewed, accepted manuscript. However, the online version of record will be different from this version once it has been copyedited and typeset.

PLEASE CITE THIS ARTICLE AS DOI: 10.1063/5.0206224

Figure 1(d) is shown in Figure 1(e). The peak at ~600 MHz represents the SAW frequency at a wavelength of $\lambda_S = 7$ µm.

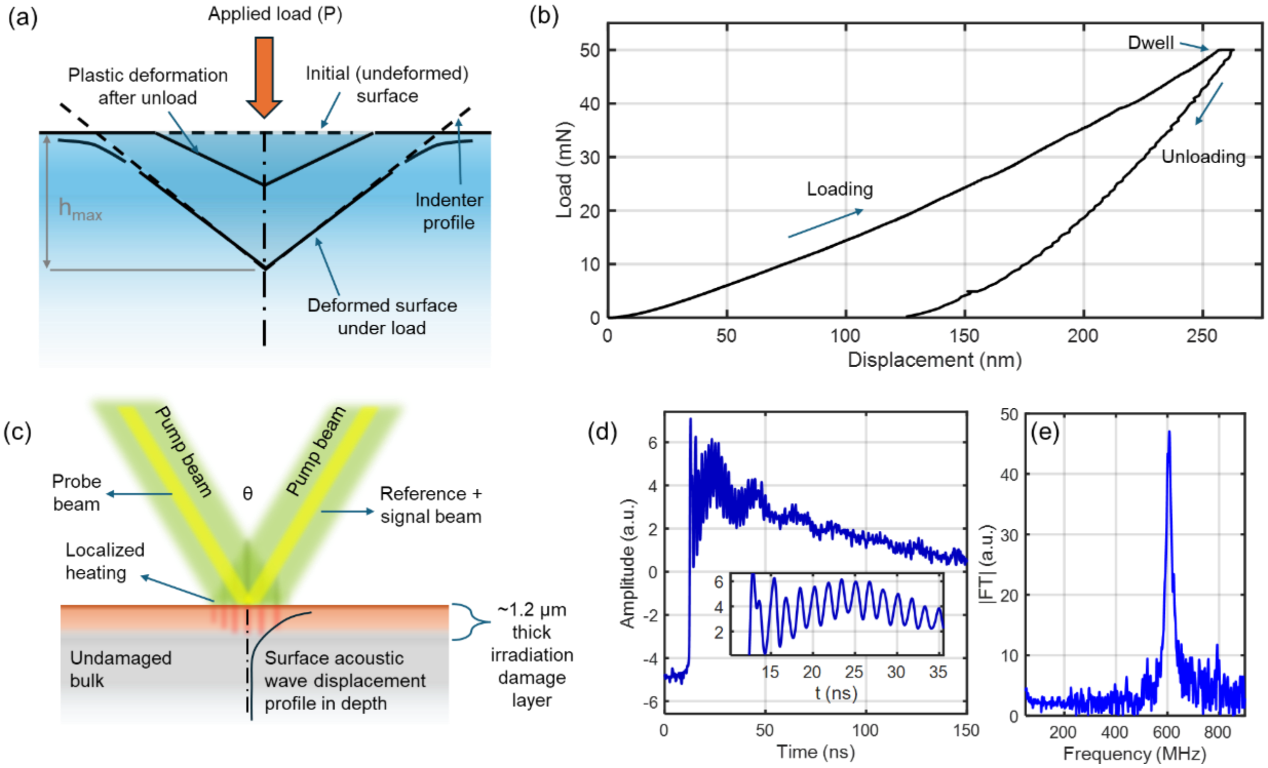

Figure 1. (a) Schematic of the nanoindentation process. The load (P) applied by the indenter deforms the surface, and leaves a plastically deformed zone following unloading. (b) Representative load versus displacement curve measured on the as-sintered $(Hf_{0.2}Nb_{0.2}Ta_{0.2}Ti_{0.2}Zr_{0.2})B_2$ high entropy diboride sample. (c) Schematic of the TGS experimental setup illustrating the generation of SAWs by spatially and temporally overlapping two laser pulses on the sample surface. The particle displacement of the SAW decays exponentially with depth, limiting the depth sensitivity to approximately the SAW wavelength λ_S. (d) Representative time-domain TGS signal acquired at a SAW wavelength $\lambda_S = 7$ µm on the quinary TM diboride $(Hf_{1/3}Ti_{1/3}Zr_{1/3})B_2$ irradiated to a fluence of 1×10^{14} Au cm^{-2}. The inset shows the high frequency oscillations associated with the SAW. (e) Fast Fourier Transform (FFT) of the SAW oscillation packet highlighting the SAW frequency peak at ~600 MHz.

TGS signals were acquired at wavelengths ranging from $\lambda_S = 4$ µm to 8.8 µm. For the case of the as-sintered (unirradiated) TM diboride samples that have uniform elastic properties in the depth, the SAWs are non-dispersive, i.e., the SAW velocity c_R can be expressed as $c_R = f \cdot \lambda_S$, where f is the frequency of the SAW oscillation packet. Since the TM diborides are also assumed to be elastically isotropic media [47], the SAW velocity c_R is approximately related to the Young's modulus E using the relation [56, 57],

$$c_R = f\lambda_S \approx (0.874 + 0.196\nu - 0.043\nu^2 - 0.055\nu^3)\sqrt{\frac{E}{2(1+\nu)\rho}} \tag{5}$$

where ν is the Poisson's ratio and ρ is the mass density. The SAW velocity c_R of the as-sintered samples is obtained from a linear fit of the frequency f versus wave number $\left(k = \frac{2\pi}{\lambda_S}\right)$ relation. The Young's modulus is then calculated by rearranging the terms in Equation (5) and using the fitted c_R and the measured density ρ. The Poisson's ratio $\nu = 0.16$ obtained from *ab initio* calculations of the elastic properties of $(Hf_{0.2}Nb_{0.2}Ta_{0.2}Ti_{0.2}Zr_{0.2})B_2$ [58] is used in Equation (5) for the calculation of the Young's

AIP Publishing
Journal of Applied Physics
ACCEPTED MANUSCRIPT
This is the author's peer reviewed, accepted manuscript. However, the online version of record will be different from this version once it has been copyedited and typeset.
PLEASE CITE THIS ARTICLE AS DOI: 10.1063/5.0206224

modulus of all four TM diboride compositions. The shear modulus G is calculated from ν and E using the relation, $G = \frac{E}{2(1+\nu)}$ [59].

Since the depth of the particle displacement associated propagating SAWs is proportional to the SAW wavelength [60, 61], the SAWs generated in the irradiated TM diborides probe both the ~1 μm thick irradiation damage layer [10] and the underlaying undamaged bulk. The differing properties between the damage layer and the undamaged bulk will induce dispersion of the SAWs (i.e., the SAW velocity will be wavelength dependent), wherein short wavelength (or high wave number) SAWs will be more sensitive to the damage layer, whereas long wavelength SAWs will have greater sensitivity to the undamaged bulk. To extract the effective elastic properties of the damage layer, the measured SAW dispersion is fitted to that predicted by an analytical model of a classical elastic layered half-space [60]. In the layered half-space model, an isotropic homogeneous solid layer (that represents the irradiation damage layer) of a fixed thickness and mass density is adhered to a semi-infinite isotropic elastic solid (that represents the unirradiated bulk). Wave propagation and elasticity equations for particle displacements, strain, and stresses must be satisfied in each medium with additional boundary conditions, namely, i) the continuity of stresses at the interface; ii) the continuity of displacements at the interface; and iii) vanishing of stresses at the free surface. The longitudinal velocity of the irradiated damage layer $c_{L,i}$ is used as a single fitting parameter in the analytical model. The Poisson's ratio is assumed to remain unchanged in the damage layer. The Young's and shear moduli of the damage layer are then calculated from the fitted values of $c_{L,i}$.

3. RESULTS AND DISCUSSION

3.1. Nanoindentation results

Representative plots of the depth-dependent hardness and indentation modulus measured using the modified CSM technique on the as-sintered and irradiated senary HEB $(Hf_{0.2}Nb_{0.2}Ta_{0.2}Ti_{0.2}Zr_{0.2})B_2$ are shown in Figure 2. The error bars represent the standard deviation across measurements acquired on multiple regions of the sample surface. The hardness shows an initial increase with penetration depth and approach a constant value above ~75 nm. This initial variation is attributed to surface effects from the initial contact between the indenter and the sample, and as such, data from the first ~75 nm are not considered. The hardness of the HEB increases from the as-sintered state to sample irradiated to a fluence of 1×10^{14} Au cm^{-2}. Samples irradiated to higher fluences, however, exhibit a monotonic reduction in hardness with ion irradiation fluence. Despite the reduction in hardness with fluence, the hardness of the HEB sample irradiated to the highest fluence of 6×10^{15} Au cm^{-2} is marginally higher than that of the as-sintered HEB. The elastic modulus of the HEB, on the other hand, exhibits an initial reduction of ~20% from the as-sintered state to the 1×10^{14} Au cm^{-2} irradiated state. Irradiating to higher fluences results in a recovery of the elastic modulus, although the elastic modulus of the sample irradiated to the highest fluence of 6×10^{15} Au cm^{-2} is ~7% lower than that of the as-sintered HEB.

ACCEPTED MANUSCRIPT

Journal of Applied Physics

AIP Publishing

This is the author's peer reviewed, accepted manuscript. However, the online version of record will be different from this version once it has been copyedited and typeset.

PLEASE CITE THIS ARTICLE AS DOI: 10.1063/5.0206224

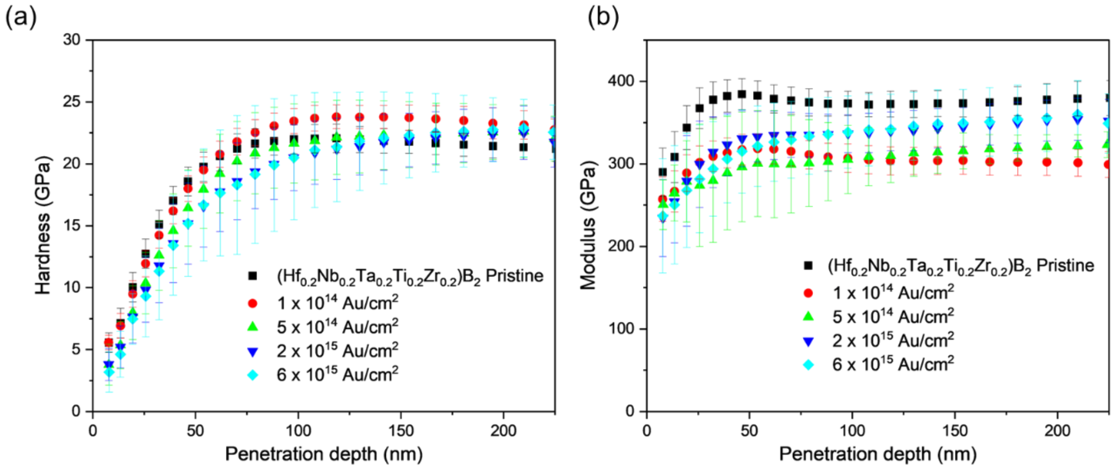

Figure 2. Depth dependence of the hardness and elastic modulus obtained using the Oliver-Pharr method [38] on the as-sintered and irradiated HEB $(Hf_{0.2}Nb_{0.2}Ta_{0.2}Ti_{0.2}Zr_{0.2})B_2$.

Table 3 lists the average hardness and Young's modulus of the as-sintered TM diborides obtained from nanoindentation tests. The average valence electron concentration (VEC) and the cation-anion electronegativity difference are also listed [10]. The nanoindentation results show that the senary high entropy diboride $(Hf_{0.2}Nb_{0.2}Ta_{0.2}Ti_{0.2}Zr_{0.2})B_2$ exhibits the highest hardness of the four samples. On the other hand, the quaternary TM diboride $(Hf_{1/3}Ta_{1/3}Zr_{1/3})B_2$ has the highest measured modulus. A recent study using first principles calculations has shown that the VEC can be correlated with the hardness and Young's modulus [31]. A higher VEC leads to an increased overlap of the transition metal $d\text{-}t_{2g}$ orbitals, that increases the Young's modulus and leads to a reduction in hardness [31]. The Young's modulus was found to reach a maximum value for TM diborides for VEC values between 8.25 to 9. In this work, discernable trends in the trade-off between hardness and elastic modulus are not manifested, likely due to the limited variation in the VEC and electronegativity difference across the four TM diboride samples.

Table 3. Average hardness and Young's modulus of as-sintered TM diborides obtained using the Oliver-Pharr method [38] for nanoindentation.

Sample	Average VEC of TMs	Electronegativity difference to anion	Hardness (GPa)	Young's modulus (GPa)
$(Hf_{1/3}Ta_{1/3}Ti_{1/3})B_2$	8.3	0.59	20.75 ± 0.793	326.25 ± 9.305
$(Hf_{1/3}Ta_{1/3}Zr_{1/3})B_2$	8.3	0.66	19.96 ± 1.088	421.94 ± 13.906
$(Hf_{1/3}Ti_{1/3}Zr_{1/3})B_2$	8.0	0.65	18.11 ± 1.034	355.95 ± 14.759
$(Hf_{0.2}Nb_{0.2}Ta_{0.2}Ti_{0.2}Zr_{0.2})B_2$	8.4	0.59	21.82 ± 1.036	372.72 ± 15.603

The hardness obtained from nanoindentation in this work is compared to previous reports of similar measurements on sintered HEBs of the same composition. The Vickers hardness of 21.7 ± 1.1 GPa measured by Zhang and coworkers on a sintered $(Hf_{0.2}Nb_{0.2}Ta_{0.2}Ti_{0.2}Zr_{0.2})B_2$ monolith [62] is in excellent agreement with the measurement in this work. While another study [63] reported a slightly lower value of the Vickers hardness (18.1 ± 1.0 GPa) for the same composition of an SPS-produced HEB monolith, the nanohardness and Young's modulus were considerably higher - 34.5 ± 0.2 GPa, and $568 - 571$ GPa, respectively [63]. This Young's modulus is consistent with other theoretical [58] and experimental studies that have calculated values of Young's modulus of $(Hf_{0.2}Nb_{0.2}Ta_{0.2}Ti_{0.2}Zr_{0.2})B_2$ to be 538 GPa (using *ab initio* methods) [58], while measurements have ranged between 448 – 544 GPa [64-66]. These values of the Young's modulus of $(Hf_{0.2}Nb_{0.2}Ta_{0.2}Ti_{0.2}Zr_{0.2})B_2$ are considerably higher than those obtained from the

AIP Publishing
Journal of Applied Physics
ACCEPTED MANUSCRIPT
This is the author's peer reviewed, accepted manuscript. However, the online version of record will be different from this version once it has been copyedited and typeset.
PLEASE CITE THIS ARTICLE AS DOI: 10.1063/5.0206224

nanoindentation measurements in this work. Further discussion on this discrepancy in the measured Young's modulus; and its comparison with that obtained from TGS measurements is provided in the following section.

Next, the effect of irradiation damage created by the energetic Au ions on the hardness and elastic modulus of the TM diborides was investigated using nanoindentation. Previous reports on radiation effects on the hardness/elastic properties of TM diborides are scarce. These include studies on the radiation stability of binary diborides that date back to over half a century [67]. A systematic understanding of radiation effects on the elastic properties of diborides has been hitherto lacking. Table 4 lists the hardness and elastic moduli of the as-sintered and ion irradiated quaternary and high entropy diborides measured using nanoindentation.

Table 4. Hardness and elastic moduli of as-sintered and irradiated TM diborides measured using nanoindentation.

Composition	Sample	Hardness (GPa)	Young's modulus (GPa)
$(Hf_{1/3}Ta_{1/3}Ti_{1/3})B_2$	As-sintered	20.75 ± 0.793	326.25 ± 9.305
	1×10^{14} Au cm^{-2}	22.03 ± 1.994	290.01 ± 20.214
	5×10^{14} Au cm^{-2}	22.32 ± 1.888	307.83 ± 16.111
	2×10^{15} Au cm^{-2}	23.49 ± 1.429	334.62 ± 18.679
	6×10^{15} Au cm^{-2}	23.51 ± 1.522	345.93 ± 13.962
$(Hf_{1/3}Ta_{1/3}Zr_{1/3})B_2$	As-sintered	19.96 ± 1.088	421.94 ± 13.906
	1×10^{14} Au cm^{-2}	24.77 ± 0.828	338.86 ± 12.852
	5×10^{14} Au cm^{-2}	23.83 ± 1.424	359.15 ± 17.875
	2×10^{15} Au cm^{-2}	23.56 ± 1.224	360.64 ± 12.629
	6×10^{15} Au cm^{-2}	23.5 ± 1.091	329.73 ± 12.839
$(Hf_{1/3}Ti_{1/3}Zr_{1/3})B_2$	As-sintered	18.11 ± 1.034	355.95 ± 14.759
	1×10^{14} Au cm^{-2}	Not available	Not available
	5×10^{14} Au cm^{-2}	Not available	Not available
	2×10^{15} Au cm^{-2}	23.95 ± 1.377	327.73 ± 20.720
	6×10^{15} Au cm^{-2}	23.64 ± 1.183	333.01 ± 21.115
$(Hf_{0.2}Nb_{0.2}Ta_{0.2}Ti_{0.2}Zr_{0.2})B_2$	As-sintered	21.82 ± 1.036	372.72 ± 15.603
	1×10^{14} Au cm^{-2}	23.76 ± 0.944	304.07 ± 16.924
	5×10^{14} Au cm^{-2}	22.86 ± 2.271	321.18 ± 12.346
	2×10^{15} Au cm^{-2}	22.62 ± 2.297	344.95 ± 22.891
	6×10^{15} Au cm^{-2}	21.94 ± 2.020	348.31 ± 40.730

For the case of all four TM diboride compositions, the hardness exhibits an initial increase after irradiation to the lowest fluence of 1×10^{14} Au cm^{-2}, followed by a subsequent reduction with increasing irradiation fluence. The quaternary TM diboride $(Hf_{1/3}Ta_{1/3}Ti_{1/3})B_2$ is a notable exception to this trend, which exhibits a rapid increase in nanohardness at low fluences, followed by a more gradual increase with increasing ion irradiation fluence. To highlight the irradiation-induced changes in hardness, the percent change in hardness (compared to the as-sintered baseline) is plotted in Figure 3. It is noted that nanoindentation data were not available on the two lowest fluences for the $(Hf_{1/3}Ti_{1/3}Zr_{1/3})B_2$ composition.

AIP Publishing
Journal of Applied Physics
ACCEPTED MANUSCRIPT
This is the author's peer reviewed, accepted manuscript. However, the online version of record will be different from this version once it has been copyedited and typeset.
PLEASE CITE THIS ARTICLE AS DOI: 10.1063/5.0206224

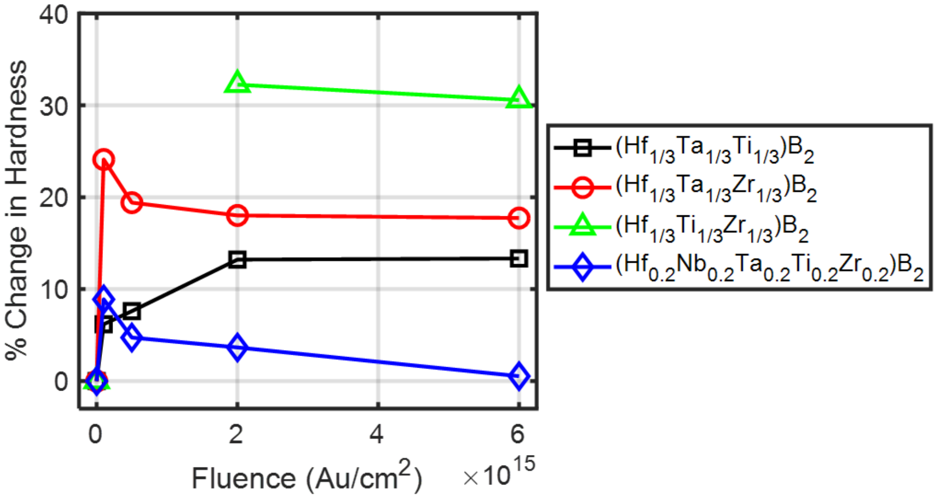

Figure 3. Percent change (relative to the as-sintered baseline) in the hardness measured using nanoindentation as a function of ion irradiation fluence for the four compositions of TM diborides.

TEM observations revealed that the low-fluence samples (i.e., 1 x 10^{14} Au/cm^2) exhibited mainly black dot dislocation loops, while the high-fluence samples (i.e., 6 x 10^{15} Au/cm^2) displayed dislocation networks [10]. Despite undergoing a volume expansion of ~4%, the TM-diborides exhibited stable crystalline structures under room-temperature irradiation and preserved the hexagonal AlB_2 phase, as seen in the XRD patterns of the irradiated TM-diborides [10]. A similar increase in the hardness following irradiation with 3 MeV Zr ions was observed in a high-entropy carbide $(Hf_{0.25}Ta_{0.25}Zr_{0.25}Nb_{0.25})C$ [68]. Like in the case of the TM-diborides investigated in this work, the high-entropy carbide retained its crystalline phase following irradiation. The microstructure comprised of perfect and faulted loops introduced by the irradiation. The observed irradiation-induced hardness increase in $(Hf_{0.25}Ta_{0.25}Zr_{0.25}Nb_{0.25})C$ was attributed to the irradiation-induced dislocation loops that hinder the slip of {111}<110> during the nanoindentations [68]. A similar hardening mechanism is observed in the irradiated TM-diborides in this work. Lattice strain, introduced from radiation-induced swelling, may also lead to an increase in hardness, as was seen in the high-entropy carbide study by Wang and coworkers [68]. At higher fluences, a high density of dislocations was observed to interconnect to form a dislocation network in the TM-diboride samples, as reported in reference 10 of the manuscript. The dislocation network does not offer additional resistance to slip motion, and therefore saturation in the measured hardness is seen at higher irradiation fluences. Of the four compositions studied here, $(Hf_{1/3}Ta_{1/3}Ti_{1/3})B_2$ showed the lowest initial increase in hardness, although it is also the only composition that showed a continued increase in hardness with irradiation fluence, suggesting the continued accumulation of point defects in its microstructure. Further analysis is needed to confirm the correlation between increased hardness and continued accumulation of small-scale defects. The HEB $(Hf_{0.2}Nb_{0.2}Ta_{0.2}Ti_{0.2}Zr_{0.2})B_2$ also exhibited a moderate increase (of ~10%) in hardness at the lowest fluence. However, unlike the quaternary TM diborides that showed a saturation with fluence, the HEB was the only composition that near-recovery to its initial hardness. This suggests that the HEB has the highest radiation resistance of the four TM diboride compositions.

3.2. TGS results

Table 5 provides the values of the Young's E and shear moduli G calculated using Equation 5 and the and the SAW speed measurements in TGS. The measured values of density (listed in Table 1) and previously reported Poisson's ratio $\nu = 0.16$ [58] were used for calculating E and G. For comparison, the values of E obtained from nanoindentation are also listed in Table 4. From the values listed in Table 5, it is clear that the Young's moduli obtained from the SAW speed measurements in TGS are notably higher than corresponding values obtained from nanoindentation. Besides the absolute values, the general

ACCEPTED MANUSCRIPT

Journal of Applied Physics

AIP Publishing

This is the author's peer reviewed, accepted manuscript. However, the online version of record will be different from this version once it has been copyedited and typeset.
PLEASE CITE THIS ARTICLE AS DOI: 10.1063/5.0206224

composition-dependent trends also do not agree. For instance, the TGS measurements show that the highest value of E (544.20 GPa) is in $(Hf_{1/3}Ti_{1/3}Zr_{1/3})B_2$, while the nanoindentation measurements show the highest value of E (421.94 GPa) is in $(Hf_{1/3}Ta_{1/3}Zr_{1/3})B_2$. The large discrepancy between the moduli obtained from TGS and nanoindentation can be attributed to length-scales of each measurement technique that differ by over two orders of magnitude. While nanoindentation probes elasticity at the sub-micrometer scale, the wavelength of the SAWs (and therefore the acoustic interrogation depth) used in this study ranged between 4 µm and 8.8 µm. Considerably lower values of Young's modulus obtained from nanoindentation may result from surface-confined porosity that locally reduces the stiffness at the sample surface. It is worth noting that the range of the elastic moduli obtained from TGS are in excellent agreement with previous calculations and measurements of the modulus of $(Hf_{0.2}Nb_{0.2}Ta_{0.2}Ti_{0.2}Zr_{0.2})B_2$ [58, 63-66].

Table 5. Young's and shear moduli obtained from the SAW speed measurements in the as-sintered TM diborides. The values of Young's modulus obtained from nanoindentation are also shown for comparison.

Sample	Young's modulus - TGS (GPa)	Shear modulus – TGS (GPa)	Young's modulus - nanoindentation (GPa)
$(Hf_{1/3}Ta_{1/3}Ti_{1/3})B_2$	517.55 ± 3.353	222.51 ± 1.44	326.25 ± 9.305
$(Hf_{1/3}Ta_{1/3}Zr_{1/3})B_2$	491.85 ± 1.47	211.46 ± 0.63	421.94 ± 13.906
$(Hf_{1/3}Ti_{1/3}Zr_{1/3})B_2$	544.20 ± 9.39	233.96 ± 4.04	355.95 ± 14.759
$(Hf_{0.2}Nb_{0.2}Ta_{0.2}Ti_{0.2}Zr_{0.2})B_2$	488.57 ± 1.70	210.05 ± 0.73	372.72 ± 15.603

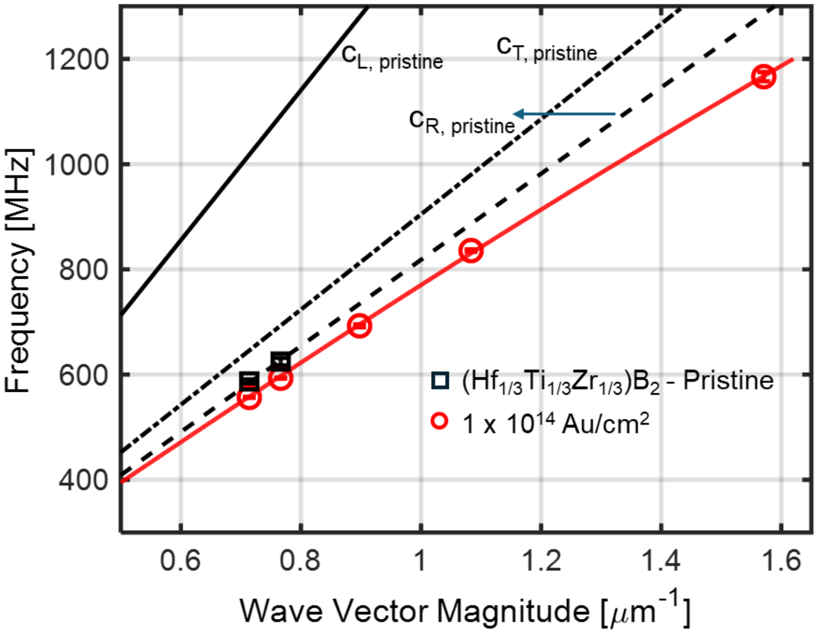

Figure 4. Measured (markers) and fitted SAW dispersion (solid red line) in $(Hf_{1/3}Ti_{1/3}Zr_{1/3})B_2$ irradiated to a fluence of 1×10^{14} Au cm^{-2}.

From the values listed in Table 5, it is clear that the Young's moduli obtained from the SAW speed measurements in TGS are notably higher than corresponding values obtained from nanoindentation. Besides the absolute values, the general composition-dependent trends also do not agree. For instance, the TGS measurements show that the highest value of E (544.20 GPa) is in $(Hf_{1/3}Ti_{1/3}Zr_{1/3})B_2$, while the nanoindentation measurements show the highest value of E (421.94 GPa) is in $(Hf_{1/3}Ta_{1/3}Zr_{1/3})B_2$.

Journal of Applied Physics
ACCEPTED MANUSCRIPT
This is the author's peer reviewed, accepted manuscript. However, the online version of record will be different from this version once it has been copyedited and typeset.
PLEASE CITE THIS ARTICLE AS DOI: 10.1063/5.0206224

Previous studies have compared the elastic moduli measured using ultrasonic techniques and nanoindentation [69, 70]. These investigations concluded that the elastic modulus of bulk samples could be measured more accurately by the ultrasonic method, since it is directly related to the elastic modulus and density. The nanoindentation technique, on the other hand, showed high precision for well-prepared, microstructurally homogeneous, and relatively hard materials but was also highly sensitive to microstructural inhomogeneities in the sample and the surface finish. The discrepancies in elastic moduli obtained from TGS and nanoindentation can therefore be attributed to length-scales of each measurement technique that differ by over an order of magnitude. Since the stress field under a point load induced by the Berkovich indenter extends to about an order of magnitude higher than the penetration depth into the sample, the elastic response may be influenced by partially by that of the unirradiated bulk, thereby providing lower values. While nanoindentation probes elasticity at the micrometer scale, the wavelength of the SAWs (and therefore the acoustic interrogation depth) used in this study ranged between 4 μm and 8.8 μm. A recent study revealed that sintered metals and ceramics exhibited a temperature gradient-induced spatial porosity variation in their microstructure [71]. The considerably lower values of Young's modulus obtained from nanoindentation may result from a combination of surface-confined porosity that locally reduces the stiffness of the sample as well as contribution to elasticity from the undamaged bulk. Detailed characterization of the spatial distribution of porosity in these samples in future investigations can support the suggested reasoning for these discrepancies. It is worth noting that the range of the elastic moduli obtained from TGS are in excellent agreement with previous calculations and measurements of the modulus of $(Hf_{0.2}Nb_{0.2}Ta_{0.2}Ti_{0.2}Zr_{0.2})B_2$ [58, 63-66].

Table 6. Young's and shear moduli of as-sintered and irradiated TM diborides obtained by fitting the measured SAW dispersion to a layered half-space model.

Composition	Sample	Young's modulus (GPa)	Shear modulus (GPa)
$(Hf_{1/3}Ta_{1/3}Ti_{1/3})B_2$	As-sintered	517.55	222.51
	1×10^{14} Au cm^{-2}	383.10	164.70
	5×10^{14} Au cm^{-2}	394.28	169.51
	2×10^{15} Au cm^{-2}	393.15	169.03
	6×10^{15} Au cm^{-2}	395.41	170.00
$(Hf_{1/3}Ta_{1/3}Zr_{1/3})B_2$	As-sintered	491.85	211.46
	1×10^{14} Au cm^{-2}	416.61	179.11
	5×10^{14} Au cm^{-2}	427.38	183.74
	2×10^{15} Au cm^{-2}	424.98	182.71
	6×10^{15} Au cm^{-2}	417.80	179.62
$(Hf_{1/3}Ti_{1/3}Zr_{1/3})B_2$	As-sintered	544.20	233.96
	1×10^{14} Au cm^{-2}	346.87	149.13
	5×10^{14} Au cm^{-2}	351.64	151.18
	2×10^{15} Au cm^{-2}	323.52	139.10
	6×10^{15} Au cm^{-2}	321.69	138.30
$(Hf_{0.2}Nb_{0.2}Ta_{0.2}Ti_{0.2}Zr_{0.2})B_2$	As-sintered	488.57	210.05
	1×10^{14} Au cm^{-2}	358.41	154.10
	5×10^{14} Au cm^{-2}	368.43	158.40
	2×10^{15} Au cm^{-2}	420.63	180.84
	6×10^{15} Au cm^{-2}	409.91	176.23

Next, the effect of irradiation damage on the Young's and shear moduli of the TM diborides was investigated using TGS. As stated in Section 2.4, since the acoustic probing depth of the SAWs exceeds

ACCEPTED MANUSCRIPT

Journal of Applied Physics

AIP Publishing

This is the author's peer reviewed, accepted manuscript. However, the online version of record will be different from this version once it has been copyedited and typeset.
PLEASE CITE THIS ARTICLE AS DOI: 10.1063/5.0206224

the irradiation damage depth estimated by SRIM, an analytical layered elastic half-space model [60] was used to fit the wavelength-dependent SAW speeds. The thickness of the irradiation damage layer was fixed at H = 1.2 µm, based on the peak ion implantation depth estimated by SRIM [10]. The density of the damage layer was fixed at 96% of the density of the as-sintered TM diborides measured using Archimedes principle [10] for all four ion irradiation fluences. This 4% reduction in density was added to account for the ~4% volume expansion previously reported in these TM diborides [10]. The longitudinal velocity $c_{L,i}$ of the 1.2 µm thick damage layer was kept as a single fitting parameter when minimizing the difference between the measured dispersion and that predicted by layered half-space analytical model. Since the damage layer and the underlaying undamaged bulk are assumed to be elastically isotropic, the fit can be optimized by manually adjusting the value of $c_{L,i}$. Such an approach has been previously reported for the extraction of effective elastic properties in a three-layer nickel/polymer/silicon sample [72]. Figure 4 shows the measured dispersion of the $(Hf_{1/3}Ti_{1/3}Zr_{1/3})B_2$ sample irradiated to 1×10^{14} Au cm^{-2} (red markers) along with the analytical layered half-space model fit (solid red line). The solid black line represents the bulk longitudinal wave line in the as-sintered $(Hf_{1/3}Ti_{1/3}Zr_{1/3})B_2$. The dash-dot and dashed black lines represent the bulk transverse wave and SAW lines, respectively. The departure of the SAW branch in the irradiated sample from the dashed SAW branch of the as-sintered sample in terms of a reduction in the slope of the SAW branch of the irradiated sample at high wave number indicates a reduction in the effective modulus of the damage layer. The Young's and shear moduli obtained from the analytical layered half-space model fits are listed in Table 6. It is noted that the Poisson's ratio was assumed to remain unchanged after ion irradiation. The fits were accurate within an uncertainty of ± 2% in the value of $c_{L,i}$.

While the hardness of the TM diborides exhibited a large initial increase at low ion irradiation fluence, followed by a saturation or gradual decrease with higher fluence, the elastic moduli exhibit a large (~30 - 37%) initial reduction at the lowest fluence, followed by a saturation or gradual continued decrease at higher fluences. The HEB $(Hf_{0.2}Nb_{0.2}Ta_{0.2}Ti_{0.2}Zr_{0.2})B_2$ is the only notable exception to this trend, where a considerable (~20%) recovery in the elastic modulus is seen at the highest fluences. Despite the discrepancy between the elastic moduli obtained from nanoindentation and TGS, the relative trends (compared to the as-sintered baseline) in the elastic moduli with irradiation fluence are examined. Figure 5 shows the percent change in the Young's modulus of the four TM diboride compositions obtained from the two measurement methods (nanoindentation and TGS) as a function of irradiation fluence. The results from nanoindentation are shown with open markers and solid lines, while the TGS results are represented with filled markers and dashed lines.

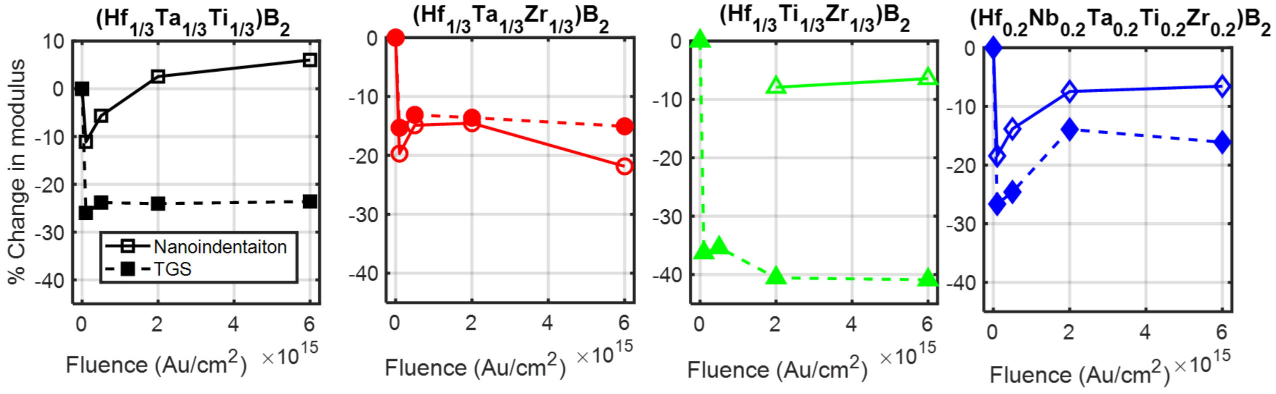

Figure 5. Percent change in the Young's modulus as a function of irradiation fluence measured using two techniques – nanoindentation (open markers, solid lines) and TGS (filled markers, dashed lines) for the four TM diboride compositions.

AIP Publishing
Journal of Applied Physics
ACCEPTED MANUSCRIPT
This is the author's peer reviewed, accepted manuscript. However, the online version of record will be different from this version once it has been copyedited and typeset.
PLEASE CITE THIS ARTICLE AS DOI: 10.1063/5.0206224

From Figure 5, it is evident that despite the large discrepancy between modulus values obtained from TGS and nanoindentation, the general trend in terms of the change in modulus with irradiation fluence agrees well between measurements obtained from the two metrology approaches with differing characteristic length-scales. The $(Hf_{1/3}Ta_{1/3}Ti_{1/3})B_2$ composition is an exception to this general trend, where the TGS measurements show a large (~30%) reduction in modulus at the lowest fluence followed by a saturation with increasing fluence, the nanoindentation results show an initial reduction of only ~10%, followed by a monotonic increase in the modulus past the original elastic modulus of the as-sintered sample. While this discrepancy may stem from a spatially heterogenous distribution of porosity and/or lattice defects, further characterization is needed to explain the measured trend between the nanoindentation and TGS techniques. The quaternary TM diboride $(Hf_{1/3}Ta_{1/3}Zr_{1/3})B_2$ (shown in red in Figure 5) and the senary HEB $(Hf_{0.2}Nb_{0.2}Ta_{0.2}Ti_{0.2}Zr_{0.2})B_2$ (shown in blue in Figure 5) also show good agreement in the absolute values of the percent change in modulus as a function of irradiation fluence. The changes in elastic moduli can be ascribed to lattice parameter changes and reduction in the bonding network created by point defects [73]. In general, the elastic moduli measured by TGS exhibited a saturation with irradiation fluence for the three quaternary TM diborides, while the elastic modulus of the HEB showed a notable recovery at high fluence after the initial reduction at low fluence. The saturation in the elastic modulus with fluence in the quaternary TM diborides corresponds to the saturation of the volume expansion reported previously in $(Hf_{1/3}Ti_{1/3}Zr_{1/3})B_2$ [10], which is caused by elastic relaxation due to the formation of interconnected networks at low fluences [74, 75]. The HEB sample on the other hand, did not show a saturation in volume expansion at low fluence, which indicates that a lower density of dislocation network forms at the same fluence when compared to that in the quaternary TM diborides. Radiation-induced point defects in the HEB, present in the microstructure before they cluster into extended defect networks, may act as pinning points for dislocations that effectively stiffen the lattice and lead to a recovery of elastic modulus at high fluences. A detailed visualization and analysis of the microstructure of TM-diborides containing only Group IVB TM-cations against those containing mixed Group IVB and VB TM-cations will further elucidate the microstructural mechanisms for the recovery of elastic modulus at high fluences. The notable recovery in the elastic modulus of the HEB at high fluence, however, suggests that this composition has higher radiation tolerance when compared to its quaternary counterparts. A similar recovery is also seen in the hardness of the HEB at high fluence.

The measurements of the changes in the hardness and elastic moduli of three quaternary TM diborides and one senary HEB after irradiation with energetic ions shed light on their radiation response. Since mechanical properties are strongly affected by lattice defects (point defects and extended defect clusters), trends in the hardness and moduli with irradiation dose offer an indirect approach to estimating the population of radiation-induced defects in the microstructure of these ceramics. The limited variation in the VEC between the four TM diboride compositions investigated here makes it difficult to correlate the nature of the chemical bond between the TM cations and the boron anion (whether metallic, ionic, or covalent or a combination thereof) to the hardness and elastic modulus. Nevertheless, the trends in the change in hardness and elastic modulus show that the addition of chemical complexity can make the material more radiation resistant (as is evidenced by the near-recovery in elastic modulus and hardness in the HEB composition). The saturation in hardness and elastic modulus with irradiation fluence indicates that even in quaternary TM diborides, lattice distortions from cation size variations may suppress further defect generation at high fluences. The aspect of element-specific tunability offers further avenues to tailor mechanical responses of HECs under irradiation.

4. SUMMARY AND CONCLUSIONS

This study provides a preliminary study of the effects of structural damage introduced by ion irradiation on the hardness and elastic properties of chemically complex transition metal diborides. The compositions investigated in this work include three quaternary transition metal diborides $(Hf_{1/3}Ta_{1/3}Ti_{1/3})B_2$, $(Hf_{1/3}Ta_{1/3}Zr_{1/3})B_2$ and $(Hf_{1/3}Ti_{1/3}Zr_{1/3})B_2$ and one senary high entropy transition metal

AIP Publishing
Journal of Applied Physics
ACCEPTED MANUSCRIPT
This is the author's peer reviewed, accepted manuscript. However, the online version of record will be different from this version once it has been copyedited and typeset.
PLEASE CITE THIS ARTICLE AS DOI: 10.1063/5.0206224

diboride $(Hf_{0.2}Nb_{0.2}Ta_{0.2}Ti_{0.2}Zr_{0.2})B_2$. Room temperature ion irradiation is performed on these diborides using 10 MeV Au ions, covering a wide range of fluences from 1×10^{14} to 6×10^{15} cm^{-2}. While previous investigations on simpler diborides have shown that tailoring the valence electron concentration and relative electronegativity difference between the cation and anion sublattices can be used to tune the ductile/brittle transition in such materials, the limited variation in VEC in the compositions investigated in this work preclude the discrimination of such effects. Hardness measurements were performed using nanoindentation, while elastic modulus measurements were performed using nanoindentation and laser-generated surface acoustic wave dispersion at two differing measurement length-scales. While the TM diborides showed an initial increase in hardness, attributed to the generation of lattice defects, the high entropy TM diboride showed a near recovery in hardness at high fluences. Considerable discrepancies were seen in the elastic moduli obtained from nanoindentation and from SAW dispersion. The agreement in the elastic moduli obtained from SAW measurements and from previous studies indicates that the unusually low values of modulus measured by nanoindentation can be tied to surface-confined porosity. The high entropy TM diboride sample shows superior radiation performance in terms of its elastic modulus when compared to quaternary TM diborides. Although a full recovery of elastic modulus in the HEB sample is not seen at high fluence, the HEB sample is the only composition that shows a trend towards elastic modulus recovery while the quaternary TM diborides show a general saturation in modulus with irradiation fluence.

Future investigations that tie characterization of radiation-induced defects to elastic properties will provide the foundation for a mechanistic understanding of the effect of radiation defect type and population on elastic properties. This study also provides pathways for further investigating the role of chemical complexity at the atomic scale on macroscopic physical properties that include hardness and elastic modulus, not just at room temperature, but also at elevated temperature and under intense radiation fields.

5. ACKNOWLEDGEMENTS

This work was supported as part of the Laboratory Directed Research and Development Program at Idaho National Laboratory under the Department of Energy (DOE) Idaho Operations Office (an agency of the U.S. Government) Contract DE-AC07-05ID145142. Ion beam work was performed at the Ion Beam Materials Laboratory located on the campus of the University of Tennessee-Knoxville. A.K. thanks M. Abi Ghanem for useful discussions relating to surface acoustic wave dispersion.

6. CONFLICT OF INTEREST STATEMENT

On behalf of all authors, the corresponding authors state that there is no conflict of interest.

7. REFERENCES

1. Brechtl, J. and P.K. Liaw, *High-entropy materials: Theory, experiments, and applications*. 2021: Springer.
2. George, E.P., D. Raabe, and R.O. Ritchie, *High-entropy alloys.* Nature reviews materials, 2019. **4**(8): p. 515-534.
3. Ma, Y., et al., *High-entropy energy materials: challenges and new opportunities.* Energy & Environmental Science, 2021. **14**(5): p. 2883-2905.
4. Zhang, Y., T. Egami, and W.J. Weber, *Dissipation of radiation energy in concentration solid-solution alloys: Unique defect properties and microstructural evolution.* Mrs Bulletin, 2019. **44**: p. 798-811.

AIP Publishing
Journal of Applied Physics
ACCEPTED MANUSCRIPT
This is the author's peer reviewed, accepted manuscript. However, the online version of record will be different from this version once it has been copyedited and typeset.
PLEASE CITE THIS ARTICLE AS DOI: 10.1063/5.0206224

5. Zhang, Y., Y.N. Osetsky, and W.J. Weber, *Tunable chemical disorder in concentrated alloys: defect physics and radiation performance.* Chemical Reviews, 2021. **122**(1): p. 789-829.
6. Oses, C., C. Toher, and S. Curtarolo, *High-entropy ceramics.* Nature Reviews Materials, 2020. **5**(4): p. 295-309.
7. Wang, F., F. Monteverde, and B. Cui, *Will high-entropy carbides and borides be enabling materials for extreme environments?* International Journal of Extreme Manufacturing, 2023.
8. Rost, C., et al., *Entropy-stabilized oxides. Nat Commun 6: 8485*. 2015.
9. Gild, J., et al., *High-entropy metal diborides: a new class of high-entropy materials and a new type of ultrahigh temperature ceramics.* Scientific reports, 2016. **6**(1): p. 37946.
10. Zhang, Y., et al., *Physical Properties and Their Influence on Irradiation Damage in Metal Diborides and in High-Entropy Materials.* JOM, 2024. **76**: p. 2602 -2618.
11. Castle, E., et al., *Processing and properties of high-entropy ultra-high temperature carbides.* Scientific reports, 2018. **8**(1): p. 8609.
12. Sarker, P., et al., *High-entropy high-hardness metal carbides discovered by entropy descriptors.* Nature communications, 2018. **9**(1): p. 4980.
13. Yan, X., et al., *(Hf0. 2Zr0. 2Ta0. 2Nb0. 2Ti0. 2) C high-entropy ceramics with low thermal conductivity.* Journal of the American Ceramic Society, 2018. **101**(10): p. 4486-4491.
14. Dippo, O.F., et al., *Bulk high-entropy nitrides and carbonitrides.* Scientific reports, 2020. **10**(1): p. 21288.
15. Jin, T., et al., *Mechanochemical-assisted synthesis of high-entropy metal nitride via a soft urea strategy.* Advanced materials, 2018. **30**(23): p. 1707512.
16. Moskovskikh, D., et al., *Extremely hard and tough high entropy nitride ceramics.* Scientific reports, 2020. **10**(1): p. 19874.
17. Zhang, R.-Z., et al., *Data-driven design of ecofriendly thermoelectric high-entropy sulfides.* Inorganic chemistry, 2018. **57**(20): p. 13027-13033.
18. Gild, J., et al., *A high-entropy silicide:(Mo0. 2Nb0. 2Ta0. 2Ti0. 2W0. 2) Si2.* Journal of Materiomics, 2019. **5**(3): p. 337-343.
19. Qin, Y., et al., *A high entropy silicide by reactive spark plasma sintering.* Journal of Advanced Ceramics, 2019. **8**: p. 148-152.
20. Dong, Y., et al., *High-entropy environmental barrier coating for the ceramic matrix composites.* Journal of the European Ceramic Society, 2019. **39**(7): p. 2574-2579.
21. Ren, X., et al., *Equiatomic quaternary (Y1/4Ho1/4Er1/4Yb1/4) 2SiO5 silicate: A perspective multifunctional thermal and environmental barrier coating material.* Scripta Materialia, 2019. **168**: p. 47-50.
22. Zhao, Z., et al., *(TiZrHf) P2O7: An equimolar multicomponent or high entropy ceramic with good thermal stability and low thermal conductivity.* Journal of Materials Science & Technology, 2019. **35**(10): p. 2227-2231.
23. Chen, J., et al., *Stability and compressibility of cation-doped high-entropy oxide MgCoNiCuZnO5.* The Journal of Physical Chemistry C, 2019. **123**(29): p. 17735-17744.
24. Zhang, X., et al., *Ultra-incompressible high-entropy diborides.* The Journal of Physical Chemistry Letters, 2021. **12**(12): p. 3106-3113.
25. Huang, S., et al., *Irradiation performance of high entropy ceramics: A comprehensive comparison with conventional ceramics and high entropy alloys.* Progress in Materials Science, 2024: p. 101250.
26. Tunes, M.A., et al., *From high-entropy alloys to high-entropy ceramics: The radiation-resistant highly concentrated refractory carbide (CrNbTaTiW) C.* Acta Materialia, 2023. **250**: p. 118856.
27. Akrami, S., et al., *High-entropy ceramics: Review of principles, production and applications.* Materials Science and Engineering: R: Reports, 2021. **146**: p. 100644.
28. Xiang, H., et al., *High-entropy ceramics: Present status, challenges, and a look forward.* Journal of Advanced Ceramics, 2021. **10**: p. 385-441.

AIP Publishing
Journal of Applied Physics
ACCEPTED MANUSCRIPT
This is the author's peer reviewed, accepted manuscript. However, the online version of record will be different from this version once it has been copyedited and typeset.
PLEASE CITE THIS ARTICLE AS DOI: 10.1063/5.0206224

29. Zhang, Y., et al., *Influence of Cr content on sintering, textured structure, and properties of (Hf, Zr, Ta, Cr, Ti) B2 high-entropy boride ceramics.* Ceramics International, 2023. **49**(10): p. 16029-16037.
30. Yasuda, K., J.-M. Costantini, and G. Baldinozzi, *Radiation-Induced Effects on Materials Properties of Ceramics: Mechanical and Dimensional Properties*. 2020, Elsevier.
31. Gu, X., et al., *Sorting transition-metal diborides: New descriptor for mechanical properties.* Acta Materialia, 2021. **207**: p. 116685.
32. Lai, C.-H., et al., *Preparation and characterization of AlCrTaTiZr multi-element nitride coatings.* Surface and Coatings Technology, 2006. **201**(6): p. 3275-3280.
33. Yeh, J.-W., *Nano-structured high-entropy alloys.* Knowledge Bridge, 2003(40): p. 1-2.
34. Feng, L., W.G. Fahrenholtz, and D.W. Brenner, *High-entropy ultra-high-temperature borides and carbides: a new class of materials for extreme environments.* Annual Review of Materials Research, 2021. **51**: p. 165-185.
35. Nisar, A., et al., *A perspective on challenges and opportunities in developing high entropy-ultra high temperature ceramics.* Ceramics International, 2020. **46**(16): p. 25845-25853.
36. Zhang, Y., et al., *Dense high-entropy boride ceramics with ultra-high hardness.* Scripta Materialia, 2019. **164**: p. 135-139.
37. Zhao, F., et al., *Enhanced hardness in tungsten–substituted molybdenum diboride solid solutions by local symmetry reduction.* Materials Chemistry and Physics, 2020. **251**: p. 123188.
38. Oliver, W.C. and G.M. Pharr, *An improved technique for determining hardness and elastic modulus using load and displacement sensing indentation experiments.* Journal of materials research, 1992. **7**(6): p. 1564-1583.
39. Hofmann, F., M.P. Short, and C.A. Dennett, *Transient grating spectroscopy: An ultrarapid, nondestructive materials evaluation technique.* MRS Bulletin, 2019. **44**(5): p. 392-402.
40. Short, M.P., et al., *Applications of transient grating spectroscopy to radiation materials science.* Jom, 2015. **67**: p. 1840-1848.
41. Zhang, Y., et al., *New ion beam materials laboratory for materials modification and irradiation effects research.* Nuclear Instruments and Methods in Physics Research Section B: Beam Interactions with Materials and Atoms, 2014. **338**: p. 19-30.
42. Ziegler, J.F., M.D. Ziegler, and J.P. Biersack, *SRIM–The stopping and range of ions in matter (2010).* Nuclear Instruments and Methods in Physics Research Section B: Beam Interactions with Materials and Atoms, 2010. **268**(11-12): p. 1818-1823.
43. Weber, W.J. and Y. Zhang, *Predicting damage production in monoatomic and multi-elemental targets using stopping and range of ions in matter code: Challenges and recommendations.* Current Opinion in Solid State and Materials Science, 2019. **23**(4): p. 100757.
44. Long, Y., et al., *Effect of yttrium on phase composition and microstructure of FeCoNiAlCrB high entropy alloys.* Materials Science and Engineering: A, 2023. **873**: p. 145058.
45. Zhang, S., et al., *Thermal cycling-induced evolution of structure and local mechanical properties in metallic glass.* Journal of Alloys and Compounds, 2024. **994**: p. 174709.
46. Zhang, S., et al., *Mechanical cycling-induced evolution of structure and local mechanical properties in a PdCuNiP bulk metallic glass.* Journal of Non-Crystalline Solids, 2024. **623**: p. 122683.
47. Castaing, J., et al., *Electronic structure of transition metal diborides.* Solid State Communications, 1969. **7**(20): p. 1453-1456.
48. Vlassak, J.J. and W. Nix, *Indentation modulus of elastically anisotropic half spaces.* Philosophical Magazine A, 1993. **67**(5): p. 1045-1056.
49. Guillonneau, G., et al., *Determination of mechanical properties by nanoindentation independently of indentation depth measurement.* Journal of Materials Research, 2012. **27**(19): p. 2551-2560.
50. Zhu, P., et al., *Toward accurate evaluation of bulk hardness from nanoindentation testing at low indent depths.* Materials & Design, 2022. **213**: p. 110317.

AIP Publishing
Journal of Applied Physics
ACCEPTED MANUSCRIPT
This is the author's peer reviewed, accepted manuscript. However, the online version of record will be different from this version once it has been copyedited and typeset.
PLEASE CITE THIS ARTICLE AS DOI: 10.1063/5.0206224

51. Hurley, D.H., *Pump-probe laser ultrasonics: characterization of material microstructure.* IEEE Nanotechnology Magazine, 2019. **13**(3): p. 29-38.
52. Rogers, J.A., et al., *Optical system for rapid materials characterization with the transient grating technique: Application to nondestructive evaluation of thin films used in microelectronics.* Applied physics letters, 1997. **71**(2): p. 225-227.
53. Rogers, J.A., et al., *Optical generation and characterization of acoustic waves in thin films: Fundamentals and applications.* Annual Review of Materials Science, 2000. **30**(1): p. 117-157.
54. Dennett, C.A. and M.P. Short, *Time-resolved, dual heterodyne phase collection transient grating spectroscopy.* Applied Physics Letters, 2017. **110**(21).
55. Johnson, J.A., et al., *Phase-controlled, heterodyne laser-induced transient grating measurements of thermal transport properties in opaque material.* Journal of Applied Physics, 2012. **111**(2).
56. Beck, C.E., et al., *Correcting for contact area changes in nanoindentation using surface acoustic waves.* Scripta Materialia, 2017. **128**: p. 83-86.
57. Lim, T.C., P. Cheang, and F. Scarpa, *Wave motion in auxetic solids.* physica status solidi (b), 2014. **251**(2): p. 388-396.
58. Wang, Y.P., et al., *Ab Initio prediction of mechanical and electronic properties of ultrahigh temperature high-entropy ceramics (Hf0. 2Zr0. 2Ta0. 2M0. 2Ti0. 2) B2 (M= Nb, Mo, Cr).* physica status solidi (b), 2018. **255**(8): p. 1800011.
59. Ciarlet, P.G., *Three-dimensional elasticity*. 1988: Elsevier.
60. Ewing, W.M., W.S. Jardetzky, and F. Press, *Elastic waves in layered media.* Geologiska Föreningen i Stockholm Förhandlingar, 1958. **80**(1): p. 128-129.
61. Rayleigh, L., *On waves propagated along the plane surface of an elastic solid.* Proceedings of the London mathematical Society, 1885. **1**(1): p. 4-11.
62. Zhang, Y., et al., *Microstructure and mechanical properties of high-entropy borides derived from boro/carbothermal reduction.* Journal of the European Ceramic Society, 2019. **39**(13): p. 3920-3924.
63. Qiao, L., et al., *First-principles prediction, fabrication and characterization of (Hf0. 2Nb0. 2Ta0. 2Ti0. 2Zr0. 2) B2 high-entropy borides.* Ceramics International, 2022. **48**(12): p. 17234-17245.
64. Feng, L., et al., *Effect of Nb content on the phase composition, densification, microstructure, and mechanical properties of high-entropy boride ceramics.* Journal of the European Ceramic Society, 2021. **41**(1): p. 92-100.
65. Gu, J., et al., *Dense and pure high-entropy metal diboride ceramics sintered from self-synthesized powders via boro/carbothermal reduction approach.* Sci China Mater, 2019. **62**(12): p. 1898-909.
66. Liu, J.-X., et al., *Mechanical properties of hot-pressed high-entropy diboride-based ceramics.* Journal of Advanced Ceramics, 2020. **9**: p. 503-510.
67. Samsonov, G., et al., *Investigation of the radiation stability of borides.* Soviet Atomic Energy, 1968. **24**(2): p. 232-233.
68. Wang, F., et al., *Irradiation damage in (Zr0. 25Ta0. 25Nb0. 25Ti0. 25) C high-entropy carbide ceramics.* Acta Materialia, 2020. **195**: p. 739-749.
69. Majumdar, P., S. Singh, and M. Chakraborty, *Elastic modulus of biomedical titanium alloys by nano-indentation and ultrasonic techniques—A comparative study.* Materials Science and Engineering: A, 2008. **489**(1-2): p. 419-425.
70. Radovic, M., E. Lara-Curzio, and L. Riester, *Comparison of different experimental techniques for determination of elastic properties of solids.* Materials Science and Engineering: A, 2004. **368**(1-2): p. 56-70.
71. Hua, Z., et al., *Microstructure characterization of electric field assisted sintering (EFAS) sintered metallic and ceramic materials using local thermal diffusivity measurement.* AIP Advances, 2023. **13**(9).
72. Glushkov, E., et al., *Evaluation of effective elastic properties of nitride NWs/polymer composite materials using laser-generated surface acoustic waves.* Applied Sciences, 2018. **8**(11): p. 2319.

AIP Publishing
Journal of Applied Physics
ACCEPTED MANUSCRIPT
This is the author's peer reviewed, accepted manuscript. However, the online version of record will be different from this version once it has been copyedited and typeset.
PLEASE CITE THIS ARTICLE AS DOI: 10.1063/5.0206224

73. Clark, D., et al., *High temperature ion irradiation effects in MAX phase ceramics.* Acta Materialia, 2016. **105**: p. 130-146.
74. Florez, R., et al., *The irradiation response of ZrC ceramics under 10 MeV Au3+ ion irradiation at 800 ºC.* Journal of the European Ceramic Society, 2020. **40**(5): p. 1791-1800.
75. Zhu, Y., et al., *Microstructural damage evolution of (WTiVNbTa) C5 high-entropy carbide ceramics induced by self-ions irradiation.* Journal of the European Ceramic Society, 2022. **42**(6): p. 2567-2576.